

## Supporting Information

### **An in-situ combustion method for scale-up fabrication of BiVO<sub>4</sub> photoanodes with enhanced long-term photostability for unassisted solar water splitting**

*Abdul Qayum, Mingrui Guo, Jing Wei, Shun Dong, Xiuling Jiao, Dairong Chen\* and Ting Wang\**

†School of Chemistry & Chemical Engineering, Shandong University; National Engineering Research Center for Colloidal Materials, Shandong University, Jinan 250100, P. R. China.  
E-mail: [t54wang@sdu.edu.cn](mailto:t54wang@sdu.edu.cn), [cdr@sdu.edu.cn](mailto:cdr@sdu.edu.cn)

#### **1. Materials.**

All raw materials were used as received and without further purification. Bi(NO<sub>3</sub>)<sub>3</sub>·5H<sub>2</sub>O, MoCl<sub>5</sub> and NiSO<sub>4</sub> were received from Shanghai Macklin Biochemical Co. Ltd.. NH<sub>4</sub>VO<sub>3</sub>, FeSO<sub>4</sub>, H<sub>3</sub>BO<sub>3</sub>, KOH, NaOH, Na<sub>2</sub>SO<sub>3</sub>, ethylene glycol was obtained from Sinopharm Chemical Reagent Co. Ltd.. Vanadyl acetylacetonate (VO(acac)<sub>2</sub>) was purchased from Aladdin Industrial Corporation.

#### **2. Characterization.**

Powder X-ray diffraction (XRD) patterns were collected on a Rigaku D/Max 2200PC diffractometer with a graphite monochromator and Cu K<sub>α</sub> radiation ( $\lambda = 0.15418$  nm). Morphology and microstructure of the products were characterized by a transmission electron microscope (TEM, JEOL JEM-1011) with an accelerating voltage of 100 kV, a field emission-scanning electron microscope (FE-SEM, SU8010), and a high-resolution transmission electron microscope (HR-TEM, JEOL JEM-2100) with an accelerating voltage of 200 kV. The X-ray photoelectron spectra (XPS) were recorded on a Thermo SCIENTIFIC ESCALAB 250Xi, and the Al K<sub>α</sub> line was used as the excitation source. The Fourier Transfer Infrared (FT-IR) spectra were measured with a Bruker alpha spectrometer in the range 400–4000 cm<sup>-1</sup>. Ultraviolet-visible (UV-vis) diffuse reflectance spectra (DRS) were recorded on an Agilent Cary 100 UV-vis spectrophotometer. The thermogravimetry-mass spectrum (TG-MS) was measured with a NETZSCH STA449F3-QMS403D. The Raman spectra were measured with a micro-Raman LabRAM HR800 spectrometer. Elemental analysis was obtained by using a Perkin Elmer 240 Elemental Analyzer.

#### **3. Photoanode fabrication.**

##### **3.1 Fabrication of the COM-BiVO<sub>4</sub> and MOD-BiVO<sub>4</sub> photoanodes.**

The fabrication of COM-BiVO<sub>4</sub> involves the following steps. In a typical procedure, Bi(NO<sub>3</sub>)<sub>3</sub> (0.4 mmol) were added into 5 mL ethylene glycol with continuous stirring, and NH<sub>4</sub>VO<sub>3</sub> (0.398 mmol) were also added in 5 ml ethylene glycol with stirring. After stirring for 30 min, two clear solutions were obtained, these solutions were mixed together with magnetic stirring for another 1 h. The obtained clear yellow solution was used as precursor for the following spraying process. Different amount of the precursor can be spray-coated on the FTO substrate upon tuning the time of the spray process. The thickness of the final film can be controlled by tuning the amount of the precursor solution deposited on the FTO substrate. The optimized film thickness can be obtained by depositing the precursor with 50 μl/cm<sup>2</sup>. The heating time required to ignite the combustion process depends on the amount of the precursor solution on the substrate. Commonly, five minutes were required to ignite the combustion process with the hotplate temperature at 140 °C. As-obtained films were placed on a hot-plate which gradually heated up to 140 °C. At ~140 °C, the combustion process was ignited and a compact film tightly

connected to the FTO substrate can be obtained, as-formed films were ultimately transferred to a muffle furnace for further calcination at the temperature of 400 °C for 2 hours in air. In order to remove the excess  $V_xO_x$  from the surface, all as-prepared films were dipped in 1M NaOH solution for 30 min, then rinsing with distilled water prior to their photocurrent measurement. To obtain 3% of Mo-doping in the final product, 0.012 mmol of  $MoCl_5$  was also added in the  $NH_4VO_3$  solution, and the molar ratio of Bi: V: Mo is 100:97:3. For preparation of the MOD- $BiVO_4$ , the only difference is to use  $VO(acac)_2$  instead of  $NH_4VO_3$  as the vanadium source.

### 3.2 Deposition of cocatalysts on combustion processed COM- $BiVO_4$ photoanodes.

The deposition of the nickel iron oxide ( $NiFeO_x$ ) cocatalyst on the surface of the working electrode was achieved by the photo-assisted electrodeposition process. An electrochemical station connected with a three-electrode cell consisting of a  $BiVO_4$  working electrode, a Pt-counter electrode and an Ag/AgCl reference electrode was used for the deposition of the cocatalyst. A 300 W Xe lamp was used as the light source for the photo-electrodeposition of the cocatalyst. For Fe deposition, an aqueous solution of  $FeSO_4$  (0.1M) was used as the electrolyte for the photo-electrodeposition of Fe at 0.25V vs Ag/AgCl for 5 min. The nickel component was further deposited from an aqueous solution of  $NiSO_4$  (25 mM) at 0.25 V vs Ag/AgCl for ~ 1 min. After the photo-electrodeposition process, the as-obtained photoanodes were further calcined in a muffle furnace with temperature up to 500 °C for 2 hours.

## 4. Photoelectrochemical measurements.

An electrochemical station (CHI760E, Shanghai Chenhua Limited, China) linked with a quartz cell via a three-electrode configuration was used for the electrochemical measurements of sulfite oxidation and water oxidation. In the cell, as-prepared  $BiVO_4$  photoanodes were used as working electrode, a Pt-foil worked as the counter electrode and Ag/AgCl were used as the reference electrode. The electrolyte consists of 1 M potassium borate solution with pH adjusted to 9. In case of the sulfite oxidation, 1 M  $Na_2SO_3$  were also added inside the above solution. Backside illumination was used to measure the photoelectrochemical property of the working electrode. A 300 W Xe lamp connected with a solar filter (AM 1.5 G) was used as the light source and the intensity of the system was calibrated to 100  $mW\ cm^{-2}$  by using an optical power meter (CEL.NP2000). The linear sweep voltammetry curves were obtained by sweeping the potential in positive direction with a scan rate of 10  $mV\ s^{-1}$ . The chopped photocurrent responses at single wavelength (440 nm, intensity ~2  $mW\ cm^{-2}$ ) were measured in 1 M potassium borate solution in the presence of sulfite. The IPCE values were obtained using a monochromatic light from a single wavelength selector (CEAULIGHT, CEL QPCE3000), while the intensity was determined by the same optical power meter described above. The Mott-Schottky plots were recorded at a frequency of 1kHz and the electrochemical impedance spectroscopy (EIS) were obtained at 0.6V vs RHE with amplitude of 10 mV under 1 sun illumination.

The potential of Ag/AgCl electrode was converted to reversible hydrogen electrode (RHE) by the formula:

$$E_{(RHE)} = E_{(Ag/AgCl)} + E^0_{(Ag/AgCl)} + 0.059\ V \times pH$$

$$\text{Where } E^0_{(Ag/AgCl)} = 0.197\ V$$

## 5. PEC-PV cell design and fabrication.

### 5.1 Tandem design and side-by-side design of the PEC-PV cell.

A tandem design of the cell was fabricated as shown in Figure 4a. A 25  $cm^2$  COM- $BiVO_4$  photoanode was placed as the front layer and Si-solar cell (6  $cm^2$ ) and counter electrode (Pt foil) were placed behind the photoanode. In a side-by-side design we placed the Si-solar cell outside the electrolyte, in parallel with the photoanode, as shown in Figure 5a.

### 5.2 Fabrication of a PEC-PV device.

To fabricate a scalable device, we prepared nine pieces of the BiVO<sub>4</sub> photoanode with size of 25 cm<sup>2</sup>. These photoanodes were fixed on a plastic panel and each of them was connected to a Si solar cell (2\*3 cm<sup>2</sup>). The PV cells were placed on the edge of the panel and these solar cells were further connected with a Pt foil placed near the photoanode, as shown in Figure 5a and Figure S16.

## 6. Calculations.

6.1 Calculations of the carrier densities from the MS curves.

The carrier densities were calculated from the following equation:

$$N_D = \frac{2}{e\epsilon\epsilon_0} \left( \frac{d(1/c^2)}{dV} \right)^{-1}$$

where  $e$  is charge of electron ( $1.6 \times 10^{-19}$  C),  $\epsilon$  is dielectric constant of BiVO<sub>4</sub> ( $\sim 68$ ),  $\epsilon_0$  is permittivity of vacuum ( $8.86 \times 10^{-14}$  F cm<sup>-1</sup>),  $V$  is the applied bias (vs RHE), and  $N_D$  is donor density for n-type semiconductor. The calculated charge density for MOD-BiVO<sub>4</sub> and COM-BiVO<sub>4</sub> are  $6.9 \times 10^{19}$  cm<sup>-3</sup> and  $2.22 \times 10^{20}$  cm<sup>-3</sup> respectively.

6.2 Calculations of the charge transfer efficiency.

Charge transfer efficiencies were determined by the following formula:

$$\eta_{trans} = \frac{J_{H_2O}}{J_{SO_3}} \times 100\%$$

Here,  $J_{H_2O}$  and  $J_{SO_3}$  represent the photocurrent densities measured in 1 M potassium borate electrolyte (pH= 9) under one sun illumination ( 100 mW.cm<sup>-2</sup>) using a photoanode of 1 cm<sup>-2</sup> without and with 1M Na<sub>2</sub>SO<sub>3</sub>, respectively.

6.3 Calculations of the incident photon to current efficiency (IPCE).

The incident photon to current efficiency (IPCE) values were calculated using the following formula:

$$IPCE = \frac{j(\lambda) \times 1240}{\lambda \times P(\lambda)} \times 100\%$$

Where  $j(\lambda)$ ,  $\lambda$ , and  $P(\lambda)$  represent the photocurrent density at specific wavelength, wavelength of incident light and the power of incident light at specific wavelength, respectively.

6.4 Calculations of applied bias potential efficiency (ABPE).

The applied bias potential efficiency (ABPE) was determined by the equation given below.

$$ABPE = \frac{J_p \times (1.23 - V)}{P_L}$$

Here,  $J_p$  is the photocurrent density,  $V$  is applied potential given to working electrode while  $P_L$  is the power of incident light (100 mW cm<sup>-2</sup>). The value of 1.23V represents the potential difference between oxygen evolution reaction (OER) and hydrogen evolution reaction (HER). The area of the photoanode used is 1 cm<sup>2</sup>.

6.5 Calculations of the Faradic efficiency (FE).

$$FE(\%) = \frac{Q_{theo}}{Q_{exp}} = \frac{A \times n(\text{mol}) \times F(\text{C.mol}^{-1})}{\text{Charge passed through WE (C)}} \times 100\%$$

Where  $Q_{exp}$  is the amount of produced gas measured from gas chromatograph (GC),  $Q_{theo}$  is the amount of gas calculated from the current passed,  $n$  is the amount of produced gas in moles measured from gas chromatograph (GC),  $A$  is the number of electrons necessary to produce one molecule of H<sub>2</sub> or O<sub>2</sub>,  $F$  is the faradic constant (96485C.mol<sup>-1</sup>) and FE is the Faradic efficiency. The area of the photoanode used is 1 cm<sup>2</sup>. The amount of O<sub>2</sub> and H<sub>2</sub> gas produced were analyzed by a gas chromatograph (Bei fen Rui Li, 3420A), Ar gas is used as the carrier gas.

## 6.6 Calculations of the solar to hydrogen efficiency (STH).

STH was calculated according to the equation below:

$$STH = \frac{J_p \times 1.23V \times FE}{I_0} \times 100 \%$$

Here, FE is the Faradic efficiency,  $J_p$  is the photocurrent density achieved under one sun illumination ( $100 \text{ Mw/cm}^2$ ) using  $1 \text{ cm}^2$  electrode area and  $I_0$  is the intensity of the incident light ( $100 \text{ mW.cm}^2$ ). The value of 1.23V represents the potential difference between oxygen evolution reaction (OER) and hydrogen evolution reaction (HER).

### Supplementary Figures:

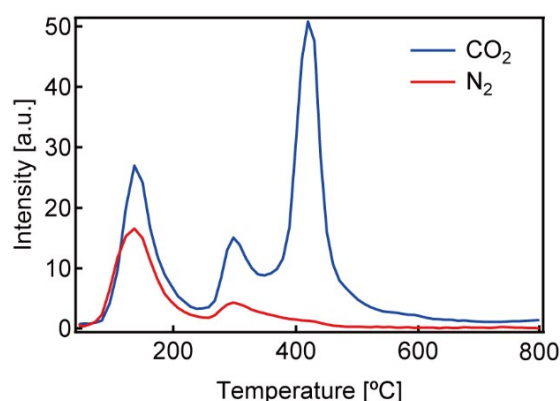


**Figure S1.** The thermogravimetry-mass spectra showing the signals of  $\text{CO}_2$  and  $\text{N}_2$  during the thermo-pyrolysis process.

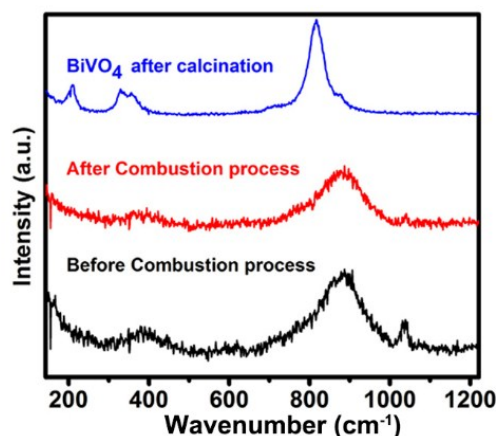


**Figure S2.** Raman spectra of the precursor before the combustion reaction (black);  $\text{BiVO}_4$  products after the combustion reaction (red) and  $\text{BiVO}_4$  products after the annealing at  $400 \text{ }^\circ\text{C}$  for 2h (blue).

The above figure shows the Raman spectra of the precursor film before and after the combustion process, and the final production after annealing. The peak at  $1040 \text{ cm}^{-1}$  which corresponds to nitrate group almost disappears after the combustion process, illustrating the apparent consumption of nitrate group during the combustion process.<sup>1</sup> For the  $\text{BiVO}_4$  sample after calcination, the bands located at  $324 \text{ cm}^{-1}$  and  $366 \text{ cm}^{-1}$  correspond to the asymmetric and symmetric vibration of V-O bond. The band at  $815 \text{ cm}^{-1}$  represents to the stretching vibration of V-O bond.<sup>2</sup> These featured bands indicate the formation of well-crystalline  $\text{BiVO}_4$  after annealing.

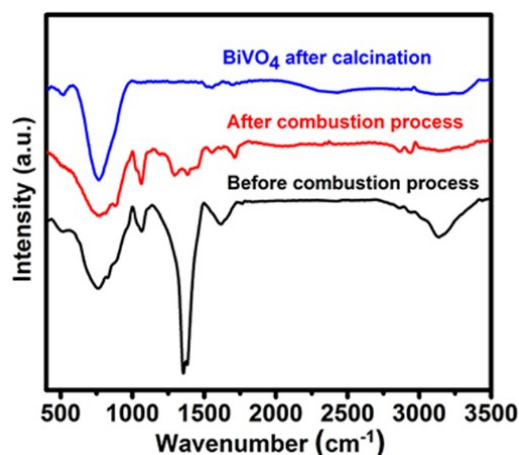


**Figure S3.** IR spectra of the precursor before the combustion reaction (black); BiVO<sub>4</sub> products after the combustion reaction (red) and BiVO<sub>4</sub> products after the annealing at 400 °C for 2h (blue).

Figure S3 shows the IR spectra of the as-prepared film before and after the combustion process and after calcination. Before the combustion process, the strong peak at ~1350 cm<sup>-1</sup> can be assigned to the antisymmetric stretch of nitrate group (-NO<sub>3</sub>).<sup>3,4</sup> After the combustion process, significant decrease in intensity occurs for that peak, indicating consumption of nitrate groups in the combustion process. With further calcination, these groups completely disappear. The peak at ~760 cm<sup>-1</sup> correspond to the (V-O) stretching mode.<sup>5</sup>

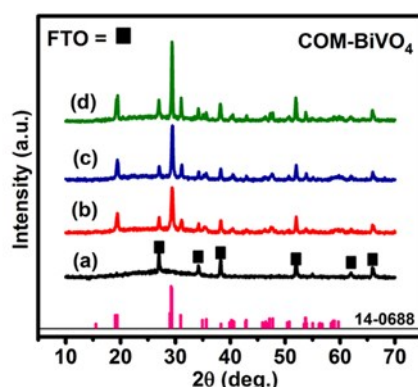


**Figure S4.** (A) XRD patterns showing the different crystallinity with different annealing temperature. (a) after combustion process at 140 °C and after calcination at (b) 200 °C(c) 300 °C(d) 400 °C.

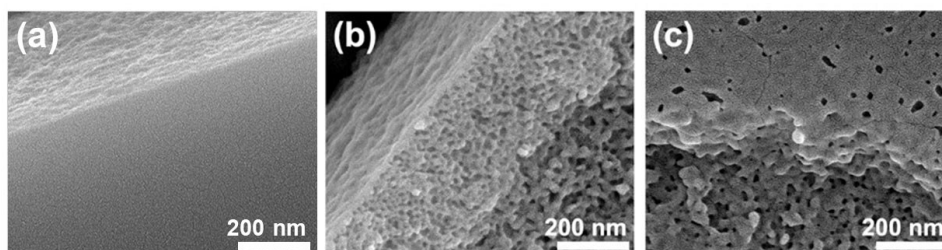


**Figure S5.** SEM images showing the evolution of the nanoporous morphology with increased annealing temperature. (a) after combustion process at 140 °C and after calcination at (b) 200 °C(c) 300 °C

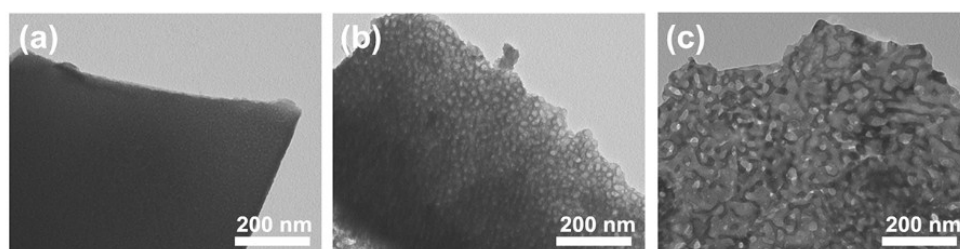


**Figure S6.** TEM images showing the evolution of the nanoporous morphology with increased annealing temperature. (a) after combustion process at 140 °C and after calcination at (b) 200 °C, (c) 300 °C.

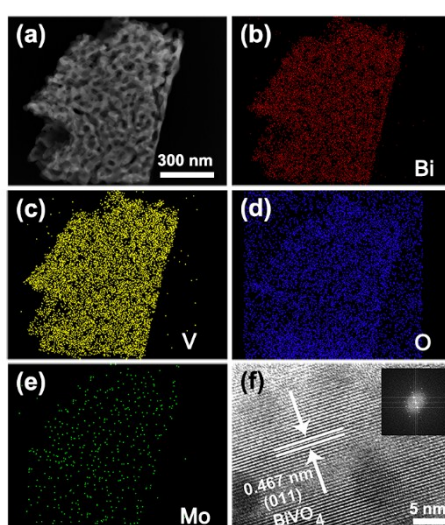


**Figure S7.** The TEM, HR-TEM images with corresponding EDX mapping showing the elemental distribution of the Mo-doped, combustion-annealing processed  $\text{BiVO}_4$  films.

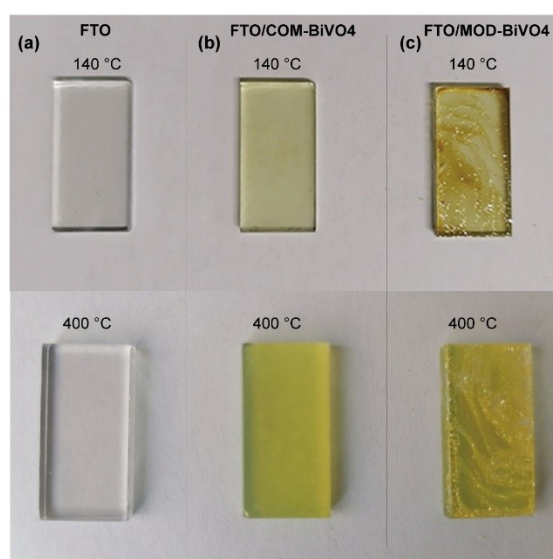


**Figure S8.** (a) Pics showing the appearance of the FTO glass after thermal treatment at 140 °C and 400 °C. (b) Appearance of the in-situ combustion processed thin  $\text{BiVO}_4$  film on FTO after

ignited at 140 °C (first row), and thermally annealed at 400 °C (second row). (c) Appearance of the MOD prepared BiVO<sub>4</sub> film on FTO after thermal evaporation of the solvent at 140 °C (first row), and annealed at 400 °C (second row).

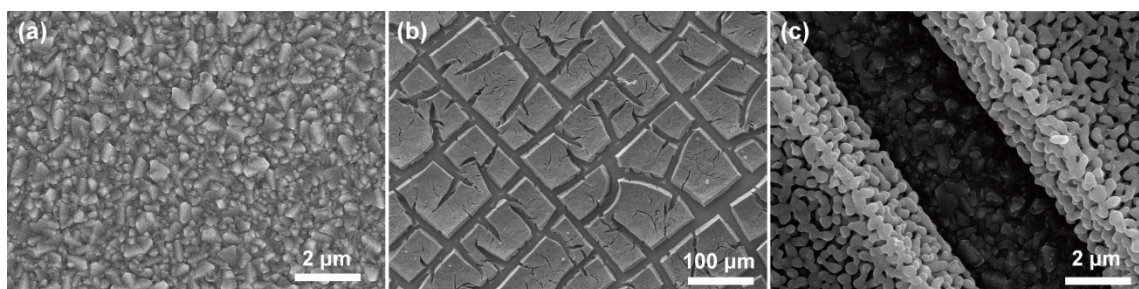


**Figure S9.** (a) SEM image showing the rough, polycrystalline surface of the FTO substrates. (b) SEM image showing the morphology of MOD prepared BiVO<sub>4</sub>, the film shrinkage upon annealing promotes the formation of lots of cracks. (c) SEM image showing a typical crack on the MOD prepared BiVO<sub>4</sub> film, the FTO substrate can be observed in the crack.

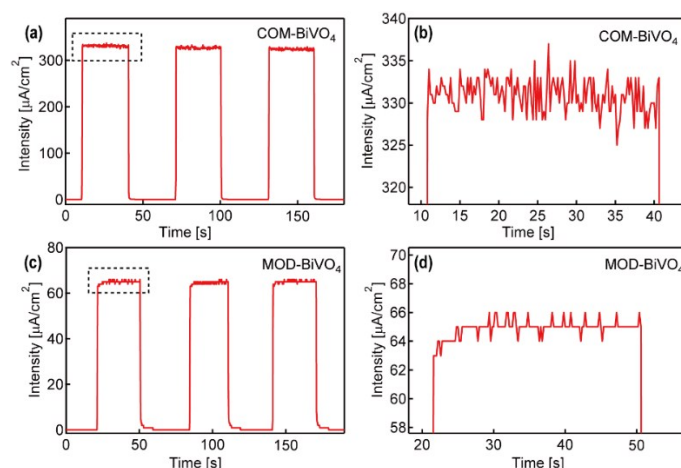


**Figure S10.** Chopped photocurrent-time plots for sulfite oxidation of (a, b) COM-BiVO<sub>4</sub>, (c, d) MOD-BiVO<sub>4</sub>. The parts of the spectra circled by the dashed line in (a) and (c) are enlarged and shown in (b) and (d).

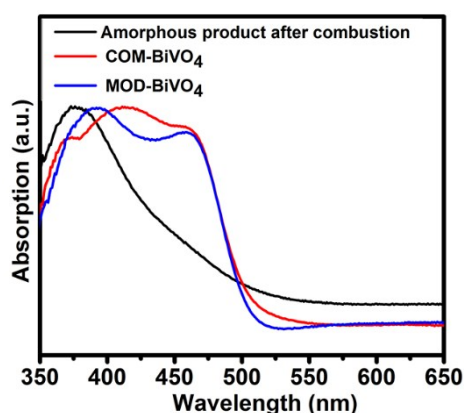


**Figure S11.** UV-vis spectra of the amorphous products after combustion process (black), crystalline COM-BiVO<sub>4</sub> (red) and crystalline MOD-BiVO<sub>4</sub> (blue).

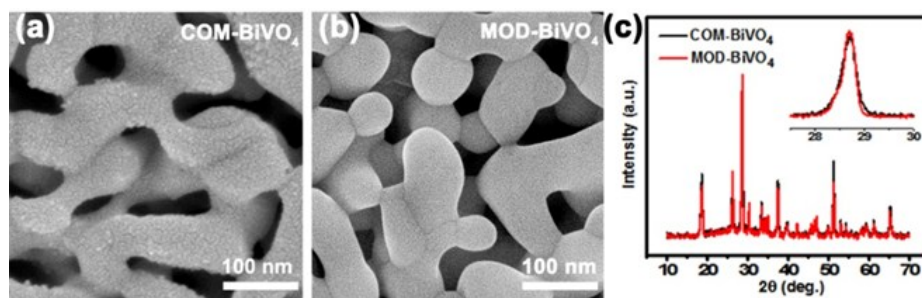


**Figure S12.** (a, b) SEM images of the COM-  $\text{BiVO}_4$  and MOD-  $\text{BiVO}_4$ , (c) The XRD patterns, showing the crystallinity of COM-  $\text{BiVO}_4$  and MOD-  $\text{BiVO}_4$ .

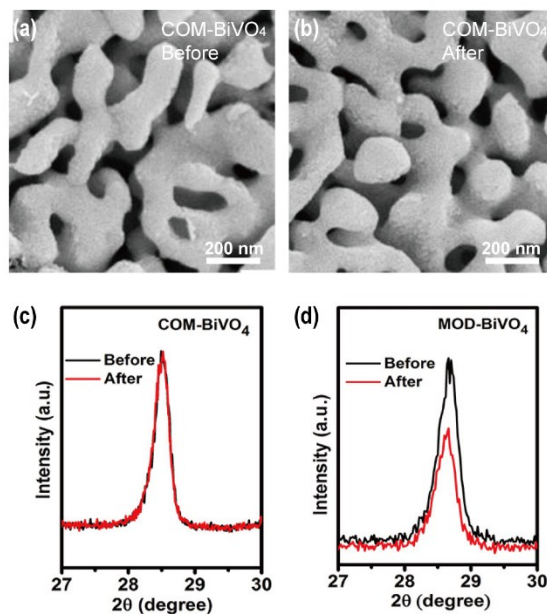


**Figure S13.** (a, b) SEM images show the surface morphology of the COM- $\text{BiVO}_4$  film before and after the long-term measurements for sulfite oxidation. (c) XRD patterns of the COM- $\text{BiVO}_4$  film before and after the long-term measurements. (d) XRD patterns of the MOD- $\text{BiVO}_4$  film before and after the long-term measurements.

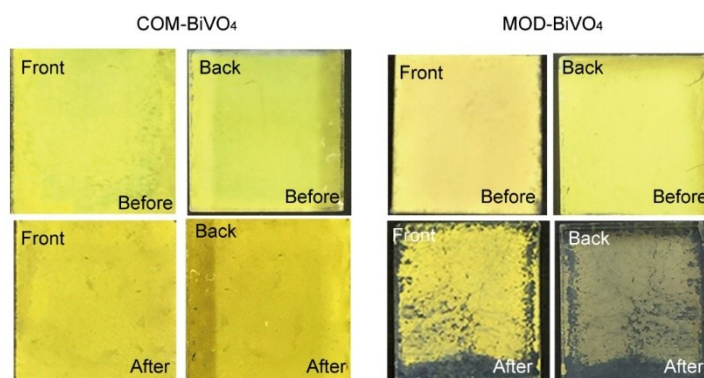


**Figure S14.** Two sets of pictures showing the appearance of the COM-  $\text{BiVO}_4$  and the MOD-  $\text{BiVO}_4$  films before and after the long-term tests towards sulfite oxidation. Front and back indicate the front side and back side of the films.

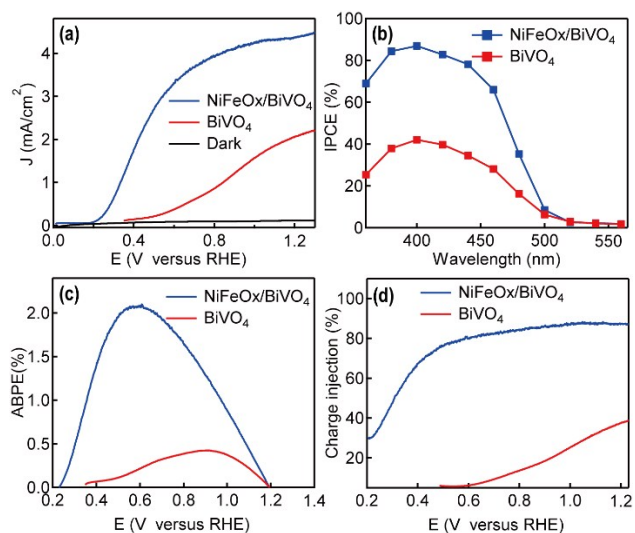


**Figure S15.** The PEC performance of the NiFeO<sub>x</sub> deposited BiVO<sub>4</sub> films for water oxidation. (a) Photocurrent density versus applied potential curves. (b) IPCE curves obtained at 1.23 V<sub>RHE</sub>. (c) ABPE curves. (d) Surface charge transfer efficiency versus applied potential curves.

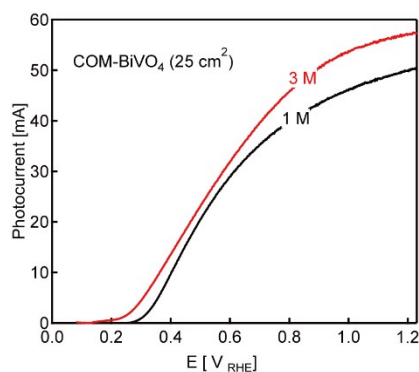


**Figure S16.** The PEC performance of the COM-BiVO<sub>4</sub> films for water oxidation in 1M and 3M borate buffer solution.

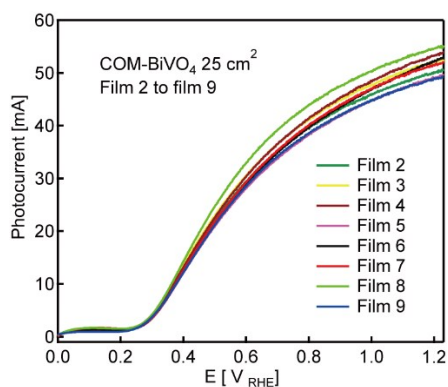


**Figure S17.** The PEC performance of the eight COM-BiVO<sub>4</sub> films for water oxidation.

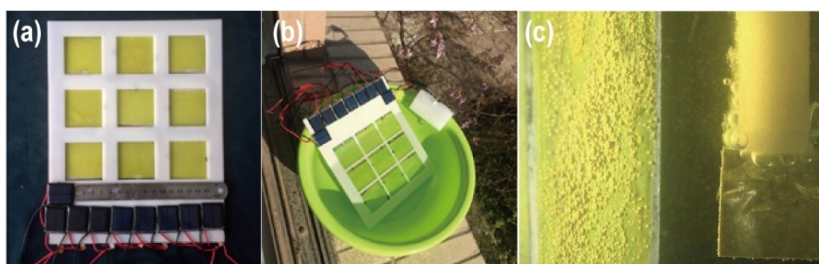


**Figure S18.** (a, b) A PEC-PV device containing 9 pieces of BiVO<sub>4</sub> photoanodes for practical unassisted solar water splitting. (c) image showing the gas bubbles attached on the surface of the BiVO<sub>4</sub> photoanode after working for ~10 min. The Pt-counter electrode is on the right part of the image.

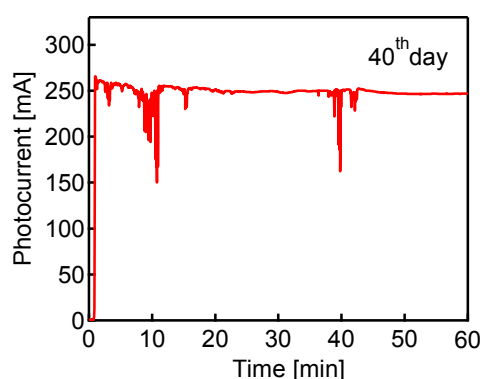


**Figure S19.** The overall photocurrent of the assembled PEC-PV device vs. time water oxidation under solar light irradiation in the 40<sup>th</sup> day of the test. The photocurrent drops in the 10 min and the 40 min periods are owing to the cloudy weather which temporarily prevented the solar irradiation. The device had been placed under solar light for ~20 min before the test begins, and there were already bubbles attached on the photoanodes, so there is no initial photocurrent drop in the curve.

**Table S1.** Comparison of our results with other reported results for scalable synthesis of BiVO<sub>4</sub> photoanode. The data is reported under one sun illumination for water oxidation.

S. No	Reference	Synthesis method	Photoanode area (cm <sup>2</sup> )	Photocurrent density (mA.cm <sup>-2</sup> )	Stability
1	Reference 2	Spin-coating, MOD	0.78 6	~3 ~1.5	Not reported
2	Reference 6	Spray-pyrolysis, Ni-lines on substrate	50	~1.2	10 min.
3	Reference 7	MOD	1 25	~1.58 ~0.8	1 h
4	Reference 8	Drop-casting, single source precursor, MOD	1 25	~1.7 ~0.8	5 h
5	Reference 9	Electrochemical synthesis	1	~1.3	6 h

			10	~1	10 h
6	This work	Solution-combustion synthesis	1 25	~4.38 ~2	~135 h (25 cm <sup>2</sup> )

## References

1. Katie L. Gares, Kyle T. Hufziger, Sergei V. Bykov, Sanford A. Asher. Review of explosive detection methodologies and the emergence of standoff deep UV resonance Raman. *J. Raman Spectrosc.* 2016,47, 124–141.
2. Simelys Hernández, Gianluca Gerardi, Katarzyna Bejtka, Alberto Fina, Nunzio Russo. Evaluation of the charge transfer kinetics of spin-coated BiVO<sub>4</sub> thin films for sun-driven water photoelectrolysis. *Applied Catalysis B: Environmental.* 2016,190, 66–74.
3. Daniel J. Goebbert, Etienne Garand, Torsten Wende, Rishu Bergmann, Gerard Meijer, Knut R. Asmis, Daniel M. Neumark. Infrared Spectroscopy of the Microhydrated Nitrate Ions NO<sub>3</sub>-(H<sub>2</sub>O)<sub>1-6</sub>. *J. Phys. Chem. A* 2009, 113, 7584–7592.
4. N. M. J. Rasali1, Y. Nagao, A. S. Samsudin. Enhancement on amorphous phase in solid biopolymer electrolyte based alginate doped NH<sub>4</sub>NO<sub>3</sub>. *Ionics.* 2019, 25, 641–654.
5. S. Daniel Abraham, S. Theodore David, R. Biju Bennie, C. Joel, D. Sanjay Kumar. Eco-friendly and green synthesis of BiVO<sub>4</sub> nanoparticle using microwave irradiation as photocatalyst for the degradation of Alizarin Red S. *Journal of Molecular Structure.* 2016,1113 174-181.
6. Ibbi Y. Ahmet, Yimeng Ma, Ji-Wook Jang, Tobias Henschel, Bernd Stannowski, Tânia Lopes, António Vilanova, Adélio Mendes, Fatwa F. Abdi, Roel van de Krol. Demonstration of a 50 cm<sup>2</sup> BiVO<sub>4</sub> tandem photoelectrochemical-photovoltaic water splitting device. *Sustainable Energy Fuels.* 2019, 3, 2366-2379.
7. Xin Yao, Danping Wang, Xin Zhao, Susu Ma, Prince S. Bassi, GuangYang, WeiChen, ZhongChen, Thirumany Sritharan. Scale-Up of BiVO<sub>4</sub> photoanode for water splitting in a photoelectrochemical cell: issues and challenges. *Energy Technol.* 2018, 6, 100–109.
8. Haijiao Lu, Virgil Andrei, Kellie J. Jenkinson, Anna Regoutz, Ning Li, Charles E. Creissen, Andrew E. H. Wheatley, Hongxun Hao, Erwin Reisner, Dominic S. Wright, Sebastian D. Pike. Single-source bismuth (Transition Metal) polyoxovanadate precursors for the scalable synthesis of doped-BiVO<sub>4</sub> photoanodes. *Adv. Mater.* 2018, 30, 1804033.
9. Andrei, V.; Hoye, R. L. Z.; Crespo-Quesada, M.; Bajada, M.; Ahmad, S.; De Volder, M.; Friend, R.; Reisner, E., Scalable Triple Cation Mixed Halide Perovskite-BiVO<sub>4</sub> Tandems for Bias-Free Water Splitting. *Advanced Energy Materials* 2018, 8 (25), 1801403.